Article

Cell Reports

Cell Type-Specific Differences in Spike Timing and Spike Shape in the Rat Parasubiculum and Superficial Medial Entorhinal Cortex

Graphical Abstract

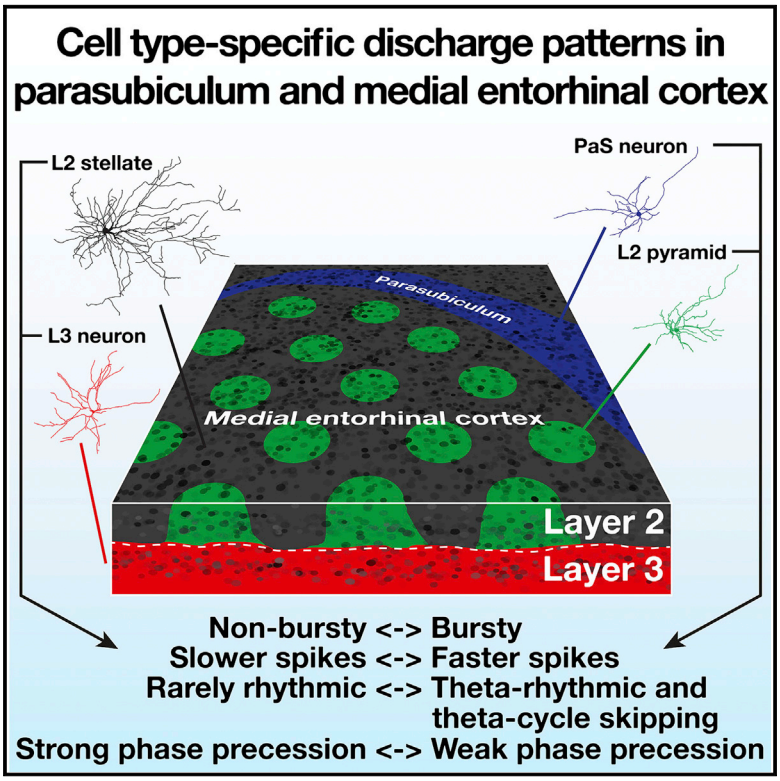

Highlights

- We find cell type-specific differences in spike shape, burstiness, and phase precession
- In vivo cell type specificity does not match predictions from previous in vitro studies
- Anatomical identity is a major determinant of spike patterns in the parahippocampal cortex

Authors

Christian Laut Ebbesen, Eric Torsten Reifenstein, Qiusong Tang, ..., Susanne Schreiber, Richard Kempter, Michael Brecht

Correspondence

michael.brecht@bccn-berlin.de

In Brief

Neurons in the parahippocampal cortex discharge in elaborate spatiotemporal firing patterns. Ebbesen et al. use juxtacellular recordings to show that the neuronal cell type is a major determinant of temporal discharge patterns such as bursting and phase precession.

Ebbesen et al., 2016, Cell Reports *16*, 1005–1015
July 26, 2016
http://dx.doi.org/10.1016/j.celrep.2016.06.057

CellPress

Cell Reports
Article

Cell Type-Specific Differences in Spike Timing and Spike Shape in the Rat Parasubiculum and Superficial Medial Entorhinal Cortex

Christian Laut Ebbesen,[1,2] Eric Torsten Reifenstein,[1,3] Qiusong Tang,[1] Andrea Burgalossi,[4] Saikat Ray,[1] Susanne Schreiber,[1,3] Richard Kempter,[1,3] and Michael Brecht[1,*]
[1]Bernstein Center for Computational Neuroscience, Humboldt Universität zu Berlin, Philippstr. 13, Haus 6, 10115 Berlin, Germany
[2]Berlin School of Mind and Brain, Humboldt Universität zu Berlin, 10115 Berlin, Germany
[3]Institute for Theoretical Biology and Department of Biology, Humboldt Universität zu Berlin, 10115 Berlin, Germany
[4]Werner Reichardt Centre for Integrative Neuroscience, Otfried-Müller-Strass 25, 72076 Tübingen, Germany
*Correspondence: michael.brecht@bccn-berlin.de
http://dx.doi.org/10.1016/j.celrep.2016.06.057

SUMMARY

The medial entorhinal cortex (MEC) and the adjacent parasubiculum are known for their elaborate spatial discharges (grid cells, border cells, etc.) and the precessing of spikes relative to the local field potential. We know little, however, about how spatio-temporal firing patterns map onto cell types. We find that cell type is a major determinant of spatio-temporal discharge properties. Parasubicular neurons and MEC layer 2 (L2) pyramids have shorter spikes, discharge spikes in bursts, and are theta-modulated (rhythmic, locking, skipping), but spikes phase-precess only weakly. MEC L2 stellates and layer 3 (L3) neurons have longer spikes, do not discharge in bursts, and are weakly theta-modulated (non-rhythmic, weakly locking, rarely skipping), but spikes steeply phase-precess. The similarities between MEC L3 neurons and MEC L2 stellates on one hand and parasubicular neurons and MEC L2 pyramids on the other hand suggest two distinct streams of temporal coding in the parahippocampal cortex.

INTRODUCTION

The discovery of grid cells in the medial entorhinal cortex (MEC) (Hafting et al., 2005) has been a major advance in cortical physiology (Burgess 2014). The assessment of single-unit activity in rats running in boxes has led to the discovery of a plethora of "functional" cell types in the MEC: conjunctive (head-directional) grid cells (Sargolini et al., 2006), border cells (Solstad et al., 2008), boundary vector cells (Koenig et al., 2011), speed cells (Kropff et al., 2015), and cue cells (Kinkhabwala et al., 2015, J Neurosci., conference). Grid and border cells also exist in areas neighboring the entorhinal cortex, such as the subiculum and pre- and parasubiculum (Lever et al., 2009; Boccara et al., 2010; Tang et al., 2016).

Computational models propose many different mechanisms to explain how grid cell discharges come about (Giocomo et al., 2011; Zilli 2012). A better knowledge of the anatomy and spatio-temporal firing patterns of defined cell types is needed to constrain models and help prune the forest of different models. Two aspects of the temporal firing patterns were highlighted in recent work: burstiness and theta cycle skipping. Burstiness has been shown to be associated with grid cell firing (Newman and Hasselmo, 2014; Latuske et al., 2015) and might serve important functions in parahippocampal microcircuits (Welday et al., 2011; Sheffield and Dombeck, 2015). Burstiness has also been linked to differences in extracellular spike shape (Newman and Hasselmo, 2014; Latuske et al., 2015). Theta cycle skipping might be related to the computation of head-directional information and grid firing (Brandon et al., 2013).

Previous investigations of burstiness and theta cycle skipping have analyzed mixed extracellular recordings from both the superficial medial entorhinal cortex and the parasubiculum (Brandon et al., 2013; Newman and Hasselmo, 2014; Latuske et al., 2015). It has thus remained unclear whether burstiness and theta cycle skipping map onto anatomical categories or whether bursty and non-bursty neurons are simply intermingled (Latuske et al., 2015). Stellate cells (Stel) in layer 2 (L2) of the medial entorhinal cortex show a tendency to fire bursts of action potentials upon membrane depolarization in vitro (Alonso and Klink, 1993; Pastoll et al., 2012; Alessi et al., 2016; Fuchs et al., 2016). Such findings led to the hypothesis that stellate cells might display bursty firing patterns in vivo (Newman and Hasselmo, 2014; Latuske et al., 2015).

Entorhinal grid cells phase-precess; i.e., they shift spike timing in a systematic way relative to the field potential during firing field transversals (Hafting et al., 2008; Jeewajee et al., 2013; Newman and Hasselmo 2014). Based on a pooled run analysis, it has been found that MEC L2 cells phase-precess more strongly than MEC layer 3 (L3) cells (Hafting et al., 2008; Mizuseki et al., 2009). This difference between MEC layers 2 and 3 has not been seen at the single run level; however, it may arise because MEC L3 cells are less correlated between runs (Reifenstein et al., 2012, 2014). Recently, a single run analysis of phase precession revealed differences between pyramidal and stellate neurons in MEC L2 (Reifenstein et al., 2016). Parasubicular neurons provide specific input to MEC L2 pyramidal neurons (Pyr) (Tang et al., 2016), but it is unknown whether parasubicular neurons phase-precess.

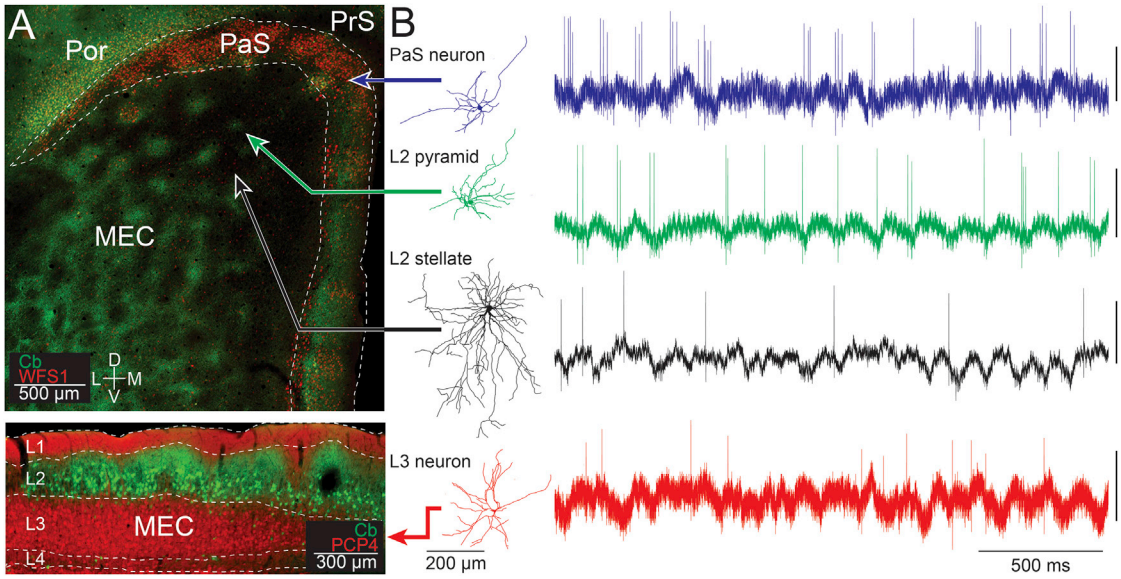

Figure 1. Parasubicular and Superficial Medial Entorhinal Cortex Neuron Types

(A) Top: tangential section of the parasubiculum (PaS) and layer 2 of the medial entorhinal cortex (MEC) stained for calbindin (Cb, green channel) and wolframin (WFS1, red channel). Bottom: parasagittal section of the MEC stained for Cb (green channel) and PCP4 (red channel). Also visible are the presubiculum (PrS) and postrhinal cortex (Por).

(B) Left: reconstructions (from tangential cortical sections; neurons are seen from the top) of examples of the four neuron types: a PaS neuron (blue), an MEC L2 pyramidal neuron (green), an MEC L2 stellate cell (black), and an MEC L3 neuron (red), corresponding to the anatomical cell types marked by arrows in (A). Right: juxtacellular recording traces of the reconstructed cells. The spiking of the parasubicular neuron and the MEC L2 pyramid is bursty and theta-modulated. Scale bars, 1 mV. Cell reconstructions were adapted from Tang et al. (2014a, 2015, 2016).

Here we analyze juxtacellular recordings from the medial entorhinal cortex (Ray et al., 2014; Tang et al., 2014a, 2015) and the parasubiculum (Tang et al., 2016). Juxtacellular data offer two advantages (Pinault 1996; Herfst et al., 2012). First, cells can often be anatomically identified. Second, juxtacellular recording of the local field potential (LFP) and spikes has a very high temporal resolution and signal-to-noise ratio, which is crucial for investigating temporal patterns such as burstiness. We ask the following questions. Does burstiness differ between parasubicular neurons, MEC L2 pyramids, MEC L2 stellates, and MEC L3 neurons? Are MEC L2 stellates actually bursty in vivo? Do differences in extracellular spike shape reflect burstiness or anatomical category? Does theta cycle skipping map onto anatomical categories? Does burstiness predict theta rhythmicity and theta locking? How does phase precession differ among cell types?

RESULTS

Overview of Anatomical Cell Types in the Parahippocampal Cortex

The parahippocampal cortex has a modular architecture. L2 of the MEC contains patches of calbindin-positive pyramidal neurons arranged in a hexagonal grid (Ray et al., 2014; Figure 1A, top) that are surrounded by calbindin-negative stellate cells (Figure 1A, top, black background). The parasubiculum (PaS) is a thin elongated structure that wraps around the MEC mediodorsally and has high wolframin expression (WFS1-positive cells; Figure 1A, top; Tang et al., 2016). Axons from the parasubiculum specifically target the patches of MEC L2 pyramidal cells (Burgalossi et al., 2011; Tang et al., 2016). MEC L3 neurons are not arranged in a hexagonal grid but are visible as a homogenous band of Purkinje cell protein 4 (PCP4)-positive cells below layer 2 (L3; red band in Figure 1A, bottom). Figure 1B, left, shows reconstructions of example cells of the four neuron types: a parasubicular neuron (blue), a MEC L2 pyramidal neuron (green), a MEC L2 stellate cell (black), and an MEC L3 pyramidal neuron (red), all recorded in freely moving rats. We use these colors throughout the manuscript. All reconstructions are from tangential sections (i.e., a "top view" of the morphology). In addition to the morphology, we also show juxtacellular recording traces from the reconstructed example cells (Figure 1B, right). Two signals are visible in the recordings: the spikes of the identified cells and the prominent theta rhythm in the LFP.

Analysis of Burstiness

To determine whether a neuron was discharging in a bursty pattern, we analyzed the interspike interval (ISI) histogram using a similar approach as Latuske et al. (2015). ISIs below 60 ms were binned in 2-ms bins (normalized to area = 1 to generate a probability distribution), which revealed that our dataset contained both non-bursty and bursty cells (Figure 2A). We performed a principal component analysis on a matrix of the ISI probability distributions of all neurons and found that the first three principal components (PCs; Figure 2B, bottom) explained 69% of the variance in the data. In agreement with Latuske et al. (2015), we found that, when the first two principal components were plotted against each other, the neurons formed a

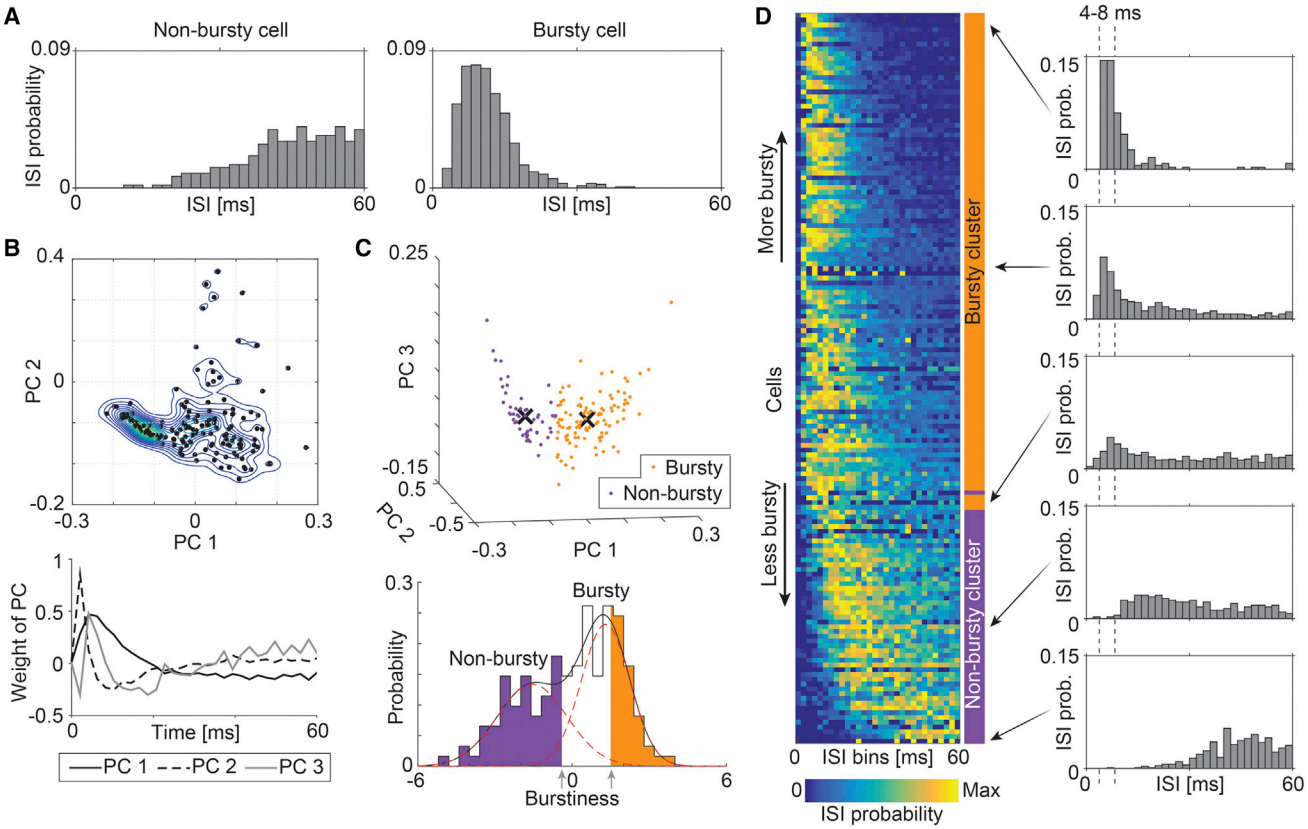

Figure 2. Classification of Bursty and Non-bursty neurons

(A) Example ISI distribution of a bursty (left) and non-bursty (right) juxtacellularly recorded neuron (bin width, 2 ms).

(B) Top: scatterplot of the first two principal components (PC1 and PC2) obtained from a PCA of ISI distributions (black dots). The neurons form a C-shaped structure, as described by Latuske et al. (2015) (2D kernel smoothed density estimate indicated by lines). Bottom: the first three PCs of the ISI histograms.

(C) Top: 3D scatterplot of the first three PCs, assigned to two clusters using a *k*-means clustering algorithm. Center-of-mass of bursty neurons (orange) and non-bursty neurons (purple) are indicated by black crosses. Bottom: projection of ISI distributions onto the optimal linear discriminant (the burstiness) of the two clusters revealed a bimodal distribution of bursty (orange) and non-bursty (purple) neurons.

(D) Left: ISI histograms of all classified neurons, sorted by burstiness (scaled to maximum probability for each neuron for visibility). Right: example ISI histograms of neurons at the edges and in the middle of the clusters. Bursty neurons tend to fire burst at 125–250 Hz (4- to 8-ms intervals).

C-shaped structure, indicative of a bimodal distribution (Figure 2B, top).

We assigned the neurons to two clusters using a *k*-means clustering algorithm on the first three principal components (Figure 2C, top). The two clusters were well separated with little overlap (Figure 2D). To assess the separation quality of the two clusters, we calculated the projection of the neurons onto Fisher's linear discriminant. We can interpret the linear discriminant as a measure of "burstiness" because it is places the cells along an axis from non-bursty to bursty based on the shape of the ISI histogram. We plotted all cells sorted according to burstiness, and, in agreement with Latuske et al. (2015), we found that bursty neurons were distinguished by a tendency to fire bursts at ~125–250 Hz (4- to 8-ms bins; Figure 2D).

To investigate differences in burstiness among cell types, we plotted the median ISI histogram of all recorded cells, resolved by cell type. The median ISI histograms of parasubicular as well as MEC L2 pyramidal neurons indicated very bursty cells (Figure 3A, top). The median ISI histograms of MEC L2 stellate and MEC L3 neurons were flat with no obvious burstiness (Figure 3A, bottom). To assess whether this difference was statistically significant, we performed two tests: one based on categorical classifications of cells as "non-bursty" and "bursty" with a guard zone (Experimental Procedures; Latuske et al., 2015) and another one where we directly compared burstiness among the neuron types.

When we compared the proportions of non-bursty, guard-zoned, and bursty cells among neuron types, we found no significant difference between parasubicular neurons and MEC L2 pyramids, which both contained predominantly bursty cells (PaS versus Pyr, bursty/guard/non-bursty: 11/11/0 versus 15/15/1, $p > 0.05$, χ^2 test; Figure 3B). We also found no difference between MEC L2 stellate cells and MEC L3 cells (Stel versus L3, bursty/guard/non-bursty: 9/25/34 versus 3/5/24, $p > 0.05$, χ^2 test; Figure 3B), which were both predominantly non-bursty. Both parasubicular neurons and MEC L2 pyramids contained significantly different proportions of bursty and non-bursty cells in comparison with both MEC L2 stellates and MEC L3 neurons (all $p < 0.001$, χ^2 tests; Figure 3B).

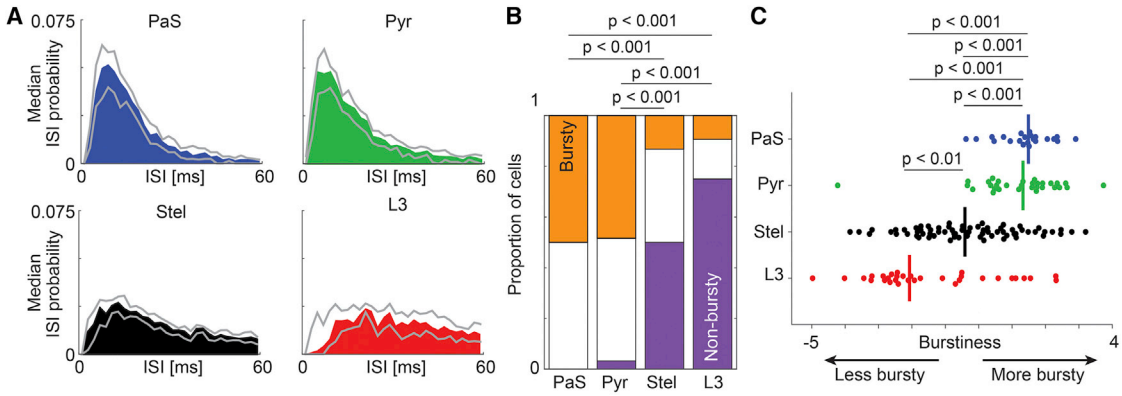

Figure 3. Burstiness in the Parasubiculum and Superficial Medial Entorhinal Cortex

(A) Median ISI histogram (bin width, 2 ms) of all neurons recorded in the PaS (blue), identified and putative MEC L2 pyramidal neurons (green), identified and putative MEC L2 stellate cells (black), and MEC L3 neurons (red). Grey lines indicate 95% confidence intervals of the median.

(B) Comparison of the proportions of the numbers of bursty (orange) and non-bursty (purple) neurons for the four different neuron types defined in (A). White areas denote cells that fall in the ambiguous zone between non-bursty and bursty (χ^2 tests of equal proportions among cell types).

(C) Comparison of the burstiness for the four different neuron types defined in (A). Vertical lines indicate medians (Mann-Whitney *U* tests).

Using a categorical classifier with a guard zone has potential problems. The width and placement of the guard zone is estimated from the bimodal fit, and thus the guard zone depends on the relative abundance of bursty and non-bursty cells, which is evidently not the same among neuron types; i.e., the guard zone might be either too wide or too narrow. The guard zone also discards information telling us whether a neuron is near the guard zone or closer to the extremes. These problems may inflate our estimated differences in burstiness among cell types. To make sure that no spurious results were imposed by the guard zone, we directly compared the burstiness of the neuron types and included all cells. In agreement with the estimations based on comparisons of the proportions, we found that the burstiness of parasubicular neurons and MEC L2 pyramids was significantly higher than the burstiness in both MEC L2 stellates and MEC L3 neurons (all $p < 0.001$, Mann-Whitney *U* tests; Figure 3C). Again, we did not find a significant difference between parasubicular neurons and MEC L2 pyramids ($p > 0.05$, Mann-Whitney *U* test; Figure 3C), but we did find that MEC L3 neurons had a significantly lower burstiness than MEC L2 stellates ($p = 0.0036$, Mann-Whitney *U* test; Figure 3C).

Thus, parasubicular neurons and MEC L2 pyramids are generally bursty, whereas MEC L2 stellates and MEC L3 neurons are generally non-bursty (Figures 3A and 3B). Furthermore, within the non-bursty neuron types, MEC L3 neurons are more strictly non-bursty than MEC L2 stellates (Figure 3C). It should be noted, however, that even though there are large and highly significant differences in burstiness among cell types, the distributions of burstiness among cell types are overlapping. For example, a minority of L2 stellate cells and L3 neurons assume firing patterns that are otherwise classically parasubicular/pyramid-like.

Our dataset includes MEC L2 neurons that were classified as putatively pyramidal or stellate based on theta strength and preferred theta phase (Tang et al., 2014a; Figure S1). We therefore also checked whether there was any correlation between burstiness and theta strength because such a correlation might introduce "artifactual" cell type differences in burstiness as a result of the classification method. First we used a statistical method. We fitted three generalized linear models to investigate whether burstiness might be related to theta strength (model 1, burstiness∼strength; Figure S3A, left), putative cell type (model 2, burstiness∼type; Figure S3A, middle), or both (model 3, burstiness∼type + strength; Figure S3A, right). Both comparisons of the Akaike information criterion (AIC; Akaike, 1974) and likelihood ratio tests of nested models indicated that model 2 is superior to the other models (Figure S3B); i.e., the burstiness depends only on putative cell type (model 2, $P_{Type} = 0.0000076$; Figure S3C, middle) and not on theta strength (model 2 versus model 3, $p = 0.54$, likelihood ratio test; Figure S3B). Second, we plotted the burstiness among cell types twice: once where we include the classified MEC L2 cells (Figure S3D, left) and once where we only include identified MEC L2 cells (Figure S3D, right). The pattern of burstiness among cell types remained the same when we only included the identified cells (Figure S3D). We thus conclude that cell type-specific differences in burstiness are not an artifact of our classification approach.

Analysis of Spike Shape

In tetrode recordings of parasubicular and MEC L2/3 neurons, differences in spike shape have been linked to burstiness (Latuske et al., 2015) and theta phase preference of grid cells (Newman and Hasselmo, 2014). We therefore investigated whether there was a difference in spike shape among our four anatomical categories of neurons. First we removed a subset of cells for which the signal-to-noise ratio of spike waveforms was insufficient to reliably assess the spike shape. Second, we removed spikes that happened within 100 ms of the previous spike to disregard potential effects of spike shape adaptation during bursts (Experimental Procedures). In Figure 4A, we plot the remaining spike shapes (normalized for display; Experimental Procedures) for all four neuron types. We did not find any differences among neuron types in spike amplitude, peak-to-trough ratio, or spike half-width (all $p > 0.05$, Kruskal-Wallis test). This

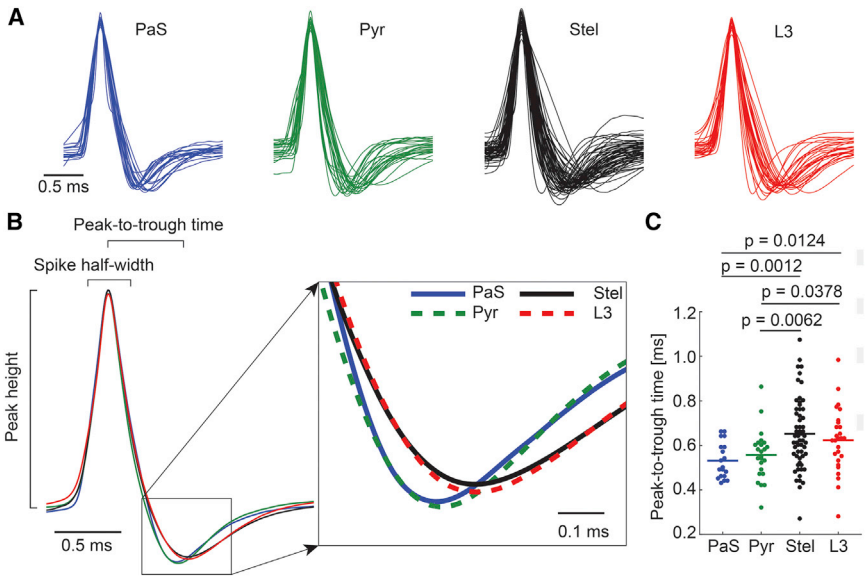

Figure 4. Spike Shapes in the Parasubiculum and Superficial Medial Entorhinal Cortex

(A) Peak-aligned and voltage-scaled spike shapes of cells in the PaS (blue), identified and putative MEC L2 pyramidal neurons (green), identified and putative MEC L2 stellate cells (black), and MEC L3 neurons (red).

(B) Left: mean spike shapes of the four neuron types in (A) show differences in peak-to-trough time. Right: close-up of the trough of the mean spike shapes.

(C) Comparison of peak-to-trough times of neurons as defined in (A) (Mann-Whitney *U* test; horizontal lines indicate means).

was expected for two reasons: Overall spike amplitude depends strongly on the particular recording pipette and relation to the soma (Gold et al., 2009), and narrow spikes and a small peak-to-trough ratio are indicative of interneurons (Mountcastle et al., 1969; Csicsvari et al., 1999), and we consider here four types of excitatory principal cells.

We noticed, however, a large variability in the repolarization phase of the cell type: Parasubicular neurons and MEC L2 pyramids contained many cells that quickly reached the trough and repolarized, whereas MEC L2 stellates and MEC L3 neurons reached the trough more slowly (Figure 4A). This tendency was also evident in the mean spike shape of the four neuron types (Figure 4B). When we compared the peak-to-trough time of the cell types, we found significant differences ($p = 0.0014$, Kruskal-Wallis test). Parasubicular neurons and MEC L2 pyramids had significantly shorter peak-to-trough times than both MEC L2 stellates and MEC L3 neurons (all $p < 0.05$, Mann-Whitney *U* test; Figure 4C).

Is Spike Shape a Reflection of Burstiness or Cell Type?

Because parasubicular neurons and MEC L2 pyramids have faster peak-to-trough times and are also the most bursty cell types, we wondered whether, as has been suggested (Latuske et al., 2015), the burstiness of the cell predicts the spike shape. Alternatively, the spike shape might simply be different among neuron types, or it might depend on neuron types as well as burstiness. To figure this out, we decided to employ a generalized linear regression approach. Because peak-to-trough time cannot assume negative values, we modeled peak-to-trough time as a gamma-distributed variable (Experimental Procedures). We selected the appropriate model using the following approach: We first modeled peak-to-trough time as a function of only burstiness (GLM1, peak-to-trough ~1 + burstiness) and found a significant dependence (ANOVA, $p_{Burstiness} = 0.0087$; Figure S4A, dashed gray line). This result is in agreement with Latuske et al. (2015). Also, when we modeled peak-to-trough time as a function of only neuron type (GLM2, peak-to-trough ~1 + type), we also found a significant dependence on neuron type (ANOVA, $p_{Type} = 0.0015$; Figure S4A, solid lines). However, when we modeled peak-to-trough time as a function of both burstiness and neuron type (GLM3, peak-to-trough ~1 + burstiness + type), we found that the dependency on type but not the dependency on burstiness remained significant (ANOVA, $p_{Burstiness} = 0.22$, $p_{Type} = 0.017$; Figure S4C). We also fitted a model where we allowed for interactions between burstiness and type (GLM4, peak-to-trough ~1 + burstiness + type + burstiness*type), where all effects became non-significant (ANOVA, all $p > 0.05$; Figure S4C). To determine which model best explains the data, we calculated the AIC of all models and found that, despite the four fitted parameters, GLM2 had the lowest AIC, indicating that the peak-to-trough time depends on neuron type, but not on burstiness (Figure S4B). Similarly, when comparing nested models, we found that GLM3 better explains the data than GLM1 ($p = 0.0023$, likelihood ratio test; Figure S4B); i.e., including neuron type as a predictor makes the model better. We did not find that GLM3 explains the data better than GLM2 ($p = 0.32$, likelihood ratio test; Figure S4B); i.e., it is unnecessary to include burstiness as a predictor in addition to neuron type. We thus infer that the differences in spike shape primarily reflect the anatomical type and not the burstiness of the neuron.

Analysis of Rhythmicity and Theta Cycle Skipping

To determine whether a neuron was theta cycle-skipping, we used a maximum likelihood estimation (MLE) of a parametric model of the ISI histogram (Climer et al., 2015; Experimental Procedures). Our dataset contained neurons that showed no theta modulation and also neurons that had strong rhythmic components (Figure 5A). For every cell, we fitted three models to the ISI distribution: a "flat" model with no rhythmic components (Figure 5A, left), a "rhythmic, non-skipping" model with a theta-rhythmic modulation of the ISI histogram (Figure 5A, middle), and a "rhythmic, cycle-skipping" model with a theta-rhythmic modulation of the ISI histogram and a second parameter introducing theta cycle skipping (i.e., a higher amplitude of every other peak in the ISI histogram; Figure 5A, right). The three fitted models were compared using the appropriate χ^2 statistic

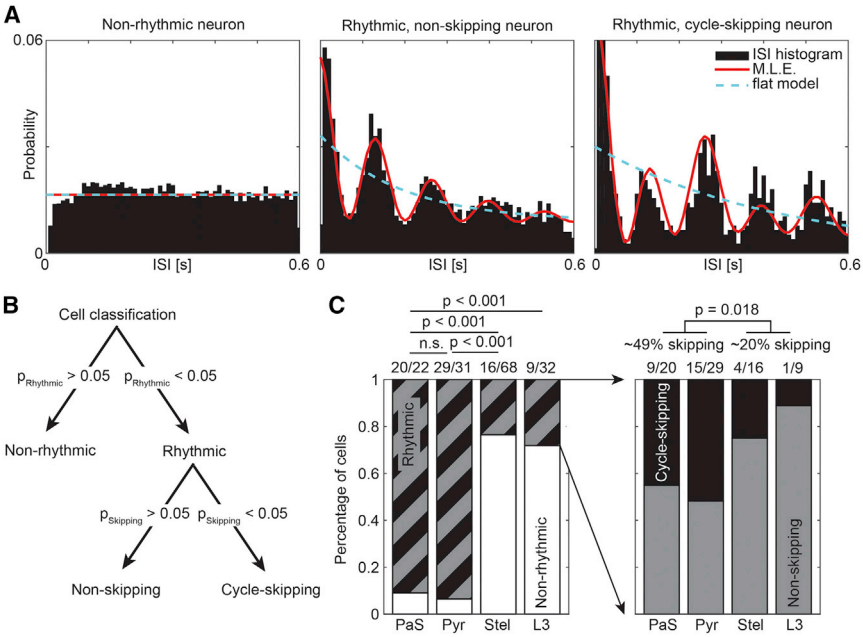

Figure 5. Theta Rhythmicity and Theta Cycle Skipping in the Parasubiculum and Superficial Medial Entorhinal Cortex

(A) Example ISI histograms (black bars) of non-rhythmic (left), rhythmic and non-skipping (middle), and rhythmic but theta cycle-skipping (right) juxtacellularly recorded neurons. Solid red lines show maximum likelihood estimates of the ISI, and dashed blue lines indicate a flat model (no rhythmicity or cycle skipping). Bin width, 1 ms.

(B) Flow diagram of the cell classification procedure. First we checked for rhythmicity and then for cycle skipping.

(C) Left: comparison of the proportions of non-rhythmic and rhythmic neurons recorded in the PaS, identified and putative MEC L2 pyramidal neurons, identified and putative MEC L2 stellate cells, and MEC L3 neurons. Right: comparison of the proportions of rhythmic, non-cycle-skipping and rhythmic, theta cycle-skipping neurons recorded in the four neuron types. The generally rhythmic cell types (PaS and Pyr) have a larger proportion of theta cycle-skipping neurons than the generally non-rhythmic cell types (Stel and L3).

(calculated from the maximum log likelihood of the models) to generate two p values: $p_{rhythmic}$ (comparing the flat and the rhythmic, non-skipping models) and $p_{skipping}$ (comparing the rhythmic, non-skipping and the rhythmic, cycle-skipping models). The cells were classified using a two-level classification (Figure 5B): First, we determined whether a cell was "rhythmic" ($p_{rhythmic}$ < 0.05) or "non-rhythmic" ($p_{rhythmic}$ > 0.05). Then we classified the rhythmic cells as either rhythmic, cycle-skipping ($p_{skipping}$ < 0.05) or rhythmic, non-skipping ($p_{skipping}$ > 0.05).

Using the MLE approach, we found that parasubicular neurons and MEC L2 pyramids were overwhelmingly rhythmic (~93%; PaS, 20/22; Pyr, 29/31; Figure 5C, left). MEC L2 stellates and MEC L3 neurons were rarely rhythmic (~26%; Stel, 16/68; L3, 9/32), both significantly less rhythmic than both parasubicular neurons and MEC L2 pyramids (all p < 0.001, χ^2 tests; Figure 5C, left). This is in agreement with previous observations in which evaluated spike train rhythmicity of cell types using a "theta index" was used (Ray et al., 2014; Tang et al., 2014a, 2016). We found that the generally rhythmic cell types were also significantly more likely to also be theta cycle-skipping than the generally non-rhythmic cell types (p = 0.018, mixed-effects logistic regression; Figure 5C, right; Experimental Procedures): Approximately 49% of the rhythmic parasubicular neurons and rhythmic MEC L2 pyramids were also theta cycle-skipping (PaS, 9/20; Pyr, 15/29; Figure 5C, right). Of the MEC L2 stellates and MEC L3 neurons, which were classified as rhythmic using the MLE approach, only ~20% were also theta cycle-skipping (Stel, 4/16; L3, 1/9; Figure 5C, right).

Our dataset includes MEC L2 neurons that were classified as putatively pyramidal or stellate based on theta strength and preferred theta phase (Tang et al., 2014a; Figure S1). Obviously, we expect a correlation between the theta rhythmicity (which is calculated from the ISI distribution) and the theta strength (locking to the LFP theta rhythm). However, the MLE approach of Climer et al. (2015) returns a p value of the rhythmicity per cell and is sensitive to very low amounts of rhythmicity, which could potentially have been present in, e.g., putative stellates with a low locking strength and locking to the peak of the LFP theta rhythm (Figure S1; Climer et al., 2015; Tang et al., 2014a). More importantly, our classification procedure considers simply strength of locking to the local LFP, and there is no way of distinguishing a simply theta-rhythmic cell from a rhythmic and cycle-skipping cell based on theta strength because they might show equally strong locking. To be sure that the cell type differences were not an artifact of including the classified cells, we plotted the burstiness among cell types twice: once where we included the classified MEC L2 cells (Figure S5A, left) and once where we only included identified MEC L2 cells (Figure S5A, right). The proportions among cell types remained the same when restricting the analysis to identified cells only (Figure S5A).

Single Run Analysis of Phase Precession

To compare the magnitude of phase precession among cell types at the single-run level, we first selected single runs of high firing based on the firing rate (Figures 6A, top, and 6B; Experimental Procedures). From these single runs, we determined the slope and range of phase precession by a circular-linear fit of time and theta phase angle of the spikes in each run (Figure 6A, bottom; Experimental Procedures). Figure 6C shows example single runs from example cells of the four neuron types. The example MEC L2 stellate and L3 neurons have steep phase precession slopes and cover larger ranges of theta phase angles during a single run. In contrast, the example parasubicular neuron and MEC L2 pyramid only weakly phase-precess. Across the population, we found the same result: First, identified and putative MEC L2 stellate and L3 neurons had approximately 3-fold steeper phase precession slopes than parasubicular neurons and identified and putative MEC L2 pyramids (Figure 6D;

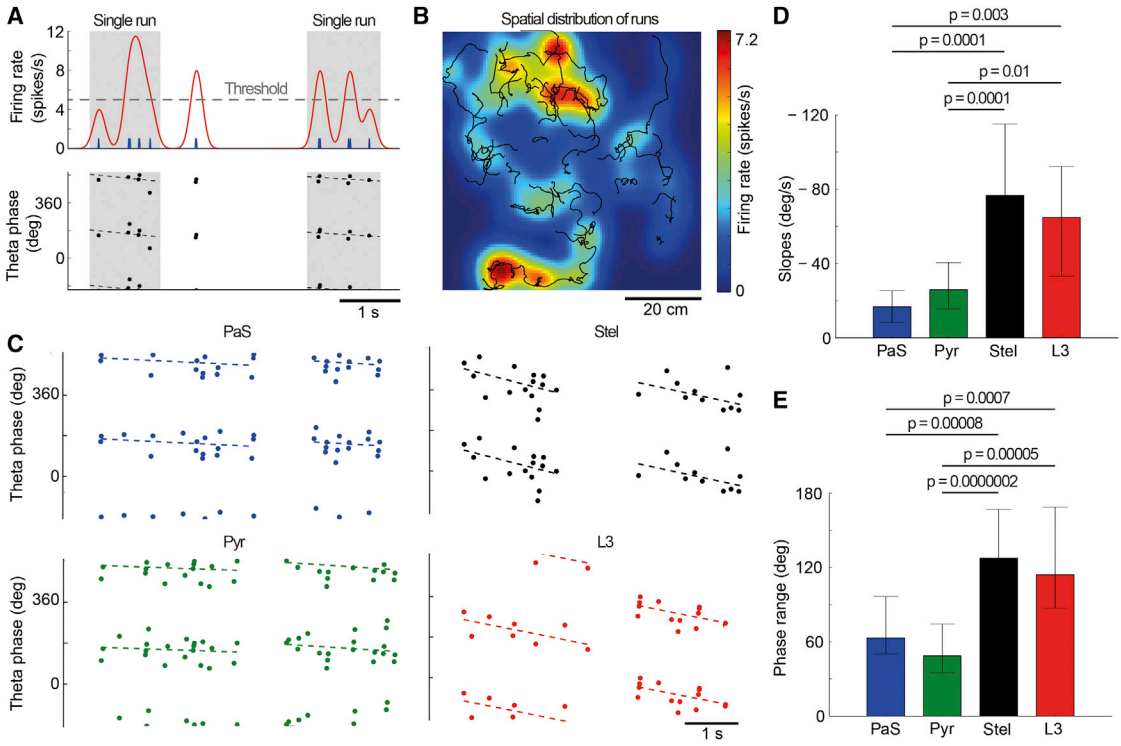

Figure 6. Phase Precession Slopes and Ranges in the Parasubiculum and Superficial Medial Entorhinal Cortex

(A) Detection of single runs. Top: firing rate (red line) is estimated by convolving spikes (blue ticks) with a Gaussian kernel. Detected runs are indicated by gray shading. Bottom: theta phase of spikes as a function of time (black dots). Phase precession slopes and ranges of single runs are estimated by circular-linear fits (dashed lines).

(B) Temporally defined single runs (black lines) match regions of elevated firing rate (color coded). Data are from the neuron shown in (A).

(C) Examples of single-run phase precession for parasubicular (blue dots), identified MEC L2 pyramidal (green dots), identified MEC L2 stellate (black dots), and MEC L3 (red dots) neurons. Each dot represents the theta phase angle of a spike as a function of time. Dashed lines depict circular-linear fits.

(D) Median single-run phase precession slopes for the four neuron types defined in (C). Single-run slopes are significantly larger in MEC L2 stellate and MEC L3 neurons than in parasubicular and MEC L2 pyramidal neurons (whiskers indicate 95% confidence intervals of the median).

(E) Median single-run phase precession ranges among the four neuron types as defined in (C) and (D). Single-run phase ranges are significantly larger in MEC L2 stellate and MEC L3 neurons than in parasubicular and MEC L2 pyramidal neurons (whiskers indicate 95% confidence intervals of the median).

median slopes: PaS/Pyr/Stel/L3 = −16.7/−25.9/−76.7/−64.8 degrees/s; p(PaS versus Stel) = 0.0001; p(PaS versus L3) = 0.003; p(Pyr versus Stel) = 0.0001; p(Pyr versus L3) = 0.01; Mann-Whitney *U* tests). Second, identified and putative MEC L2 stellate and L3 neurons covered a much larger range of theta phase angles per run than parasubicular neurons and identified and putative MEC L2 pyramids (approximately 2-fold; Figure 6E; median ranges: PaS/Pyr/Stel/L3 = 63.2/48.7/127.5/114.2 degrees; p(PaS versus Stel) = 0.00008; p(PaS versus L3) = 0.0007; p(Pyr versus Stel) = 0.0000002; p(Pyr versus L3) = 0.00005; Mann-Whitney *U* tests). We did not find any differences in the circular-linear correlation coefficient among the cell types (p = 0.38, Kruskal-Wallis test).

DISCUSSION

We used advanced statistical techniques to tease apart how differences in burstiness, spike shape, theta modulation (rhythmicity, locking, skipping), and phase precession map onto regular spiking layer 3 medial entorhinal neurons, layer 2 medial entorhinal pyramidal neurons, layer 2 medial entorhinal stellate neurons, and parasubicular regular spiking cells.

Cell Type-Specific Differences and Their Origin

We found significant differences in spike shape, burstiness, theta modulation (rhythmicity, locking, cycle skipping, phase precession), and theta phase precession between the four groups of cells investigated. Thus, our data suggest that cell type is a major determinant of discharge patterns in the rat parasubiculum and superficial medial entorhinal cortex. Although our data emphasize the significance of cell types, the discharge patterns we observed do not directly match what is expected based on the analysis of intrinsic properties of these neurons in vitro. In vitro recordings of parasubicular neurons have suggested an intrinsic disposition for theta rhythmicity (Glasgow and Chapman, 2008). It is known that in vitro measurements of L2 MEC cell properties are very sensitive to recording conditions (Alonso and Klink, 1993; Pastoll et al., 2012). However, MEC L2 stellates often display some intrinsic burstiness in vitro (Alonso and Klink, 1993; Pastoll et al., 2012; Alessi et al., 2016; Fuchs et al., 2016), but they are generally not very bursty in vivo (Ray

et al., 2014; Figure 2). Thus, it is probably incorrect to assume that bursty cells recorded extracellularly in the superficial MEC and the parasubiculum are MEC L2 stellates (Newman and Hasselmo, 2014; Latuske et al., 2015) because we show that bursty cells are more likely to be MEC L2 pyramids or parasubicular neurons.

Cell Type Specificity of Phase Precession

Although phase precession is arguably the most intensely studied example of temporal coding in the brain, its underlying mechanism is still a matter of debate. Parasubicular neurons, which show only weak phase precession, project to pyramidal cells in MEC L2 (Tang et al., 2016). Also, these MEC L2 pyramidal cells express only a low degree of phase precession. Conversely, stellate cells in MEC L2 and pyramidal cells in MEC L3 phase precess with steep slopes. The latter finding is somewhat surprising because it challenges the long-held belief that cells in MEC L3 do not phase-precess (Hafting et al., 2008; Mizuseki et al., 2009). However, differences in methodology might reconcile the different findings. Previous studies investigated MEC L3 phase precession in pooled run data. In contrast to that, we analyzed phase precession in single runs (Schmidt et al., 2009). We argue that the single-run approach is more appropriate because the animal needs to process information online and does not have the opportunity to pool over trials. Our finding of substantial MEC L3 phase precession is in line with a previous single-run account (Reifenstein et al., 2014). MEC L2 stellate cells project to the dentate gyrus, whereas MEC L2 pyramidal cells send output to CA1 (Varga et al., 2010; Kitamura et al., 2014; Ray et al., 2014). Because MEC L2 pyramidal cells show only weak phase precession, it seems unlikely that they substantially contribute to CA1 phase precession. Therefore, CA1 either generates phase precession de novo or inherits phase-precessing inputs via the strongly precessing stellate cells in MEC L3 (Jaramillo et al., 2014).

Whether Cell Types Show Specific Spatial Discharge Patterns Is Currently Unresolved

It is presently unknown how the functional categories (grid cells, border cells, speed cells, cue cells, etc.) map onto the anatomy. For example, it is unknown whether MEC L2 grid cells are predominantly pyramidal cells (Tang et al., 2014a) or stellate cells (Domnisoru et al., 2013) or whether they show no preference for either cell type (Sun et al., 2015). Similarly, some authors have reported that about a third to half of MEC L3 neurons are grid cells (Sargolini et al., 2006; Boccara et al., 2010), whereas others have estimated that if L3 grid cells exists, then they must be rare (~1%; Tang et al., 2015).

Relation between Temporal Spiking Features and Spatial Responses

Parasubicular neurons and MEC L2 pyramids are more bursty, have narrower spikes, and are more likely to be theta-rhythmic, theta-locked, and theta cycle-skipping than MEC L2 stellates and MEC L3 neurons. These differences remain even when we statistically control for interactions between spike shape, burstiness, and rhythmicity. Some studies have tried to elucidate the grid cell generation mechanism by characterizing the firing properties of the entorhinal network. From these studies we know that grid cells are bursty whereas border cells are not (Newman and Hasselmo 2014; Latuske et al., 2015). It has also been shown that theta cycle skipping is somehow necessary for maintaining grid cell firing (Brandon et al., 2013). In agreement with Tang et al. (2014a, 2016), we conclude that, based on burstiness and theta cycle skipping, parasubicular neurons and MEC L2 pyramids are likely to play a key role in generating grid cell activity in the parasubiculum and superficial medial entorhinal cortex.

Cell Type-Specific Differences in Spike Shape

In line with the differences in temporal discharge patterns, we observed that parasubicular and MEC L2 pyramidal cells had shorter spike durations than MEC L2 stellates and MEC L3 neurons. Several previous studies have noticed significant differences between MEC L2 pyramidal and MEC L2 stellate cells, most notably, that stellate cells have larger depolarizing afterpotentials (Alonso and Klink 1993; Alessi et al., 2016; Fuchs et al., 2016). In in vivo recordings, it was generally observed that stellate cells had a shorter spike duration than pyramidal cells (Alonso and Klink, 1993). Interestingly, however, it was also found that the spike duration of both pyramidal and stellate cells varied depending on the depolarizing current pulse (Alonso and Klink, 1993). Thus, the juxtacellularly observed differences in spike shape are probably not primarily a reflection of differences in intrinsic cell properties. Cell type differences in spike duration are statistically significant. However, the distributions of spike durations are largely overlapping (Figure 4C), probably precluding a classification of extracellularly recorded MEC L2 regular spiking neurons into pyramidal and stellate cells based purely on spike shape.

Do Layer 3 Cells and Layer 2 Stellate Cells, on One Hand, and Parasubiculum and Layer 2 Pyramids, on the Other Hand, Form Two Distinct Processing Systems?

We observed a strong similarity between spike shapes and firing patterns of parasubicular neurons and MEC L2 pyramids. These two neuron groups were different in spike shapes and firing patterns from layer 3 cells and layer 2 stellate cells, which were similar to each other, however. It turns out that these neurons groups share even more similarities and differences. Parasubicular axons specifically target patches of MEC L2 pyramidal cells (Tang et al., 2016), which might be a pathway for head-directional information from the medial septum to reach the grid cell system (Winter et al., 2015; Unal et al., 2015; Tang et al., 2016). L3 cells and layer 2 stellate cells provide a massive direct (L3) and indirect input to the hippocampus, whereas projections from both layer 2 pyramids and the parasubiculum are minor or absent (Varga et al., 2010; Ray et al., 2014; Kitamura et al., 2014). Thus, analysis of spike shapes and firing patterns, direct connectivity, and projection targets supports the distinction of layer 3 cells and layer 2 stellate cells on one hand and parasubiculum and layer 2 pyramids on the other hand as two distinct processing systems.

Possible Anatomical Origin of Firing Patterns

Layer 2 pyramids and parasubicular cells are anatomically similar. They both express wolframin (Ray and Brecht, 2016),

and, in the early development stages, they also express calbindin (Ray and Brecht, 2016). Likewise, layer 3 neurons and layer 2 stellate cells also have an anatomical likeliness in their protein expression profile, with both expressing Reelin in adult rats (Ray and Brecht, 2016). This might allude to the electrophysiological and functional characteristics of these two groups being perhaps somewhat genetically determined, with the protein expression profiles of these respective cell groups shaping their inputs and outputs.

Grid Cell Models

Our results will constrain future modeling of network activity in the hippocampus and para-hippocampal cortices. Because different anatomical cell types have different projection patterns, burstiness, and theta rhythmicity/skipping might be passed on differentially to hippocampal subfields like the dentate gyrus, which receives massive MEC L2 stellate input (Varga et al., 2010), and CA1, which receives some MEC L2 pyramidal input (Kitamura et al., 2014). Some grid cell models suggest that grid cells are generated by network mechanisms where a large number of similar (stellate) cells self-organize to generate symmetrical firing patterns either via continuous attractors or via oscillatory interference (for reviews, see Giocomo et al., 2011; Zilli 2012). Others have suggested mechanisms based on anatomical microcircuits (Brecht et al., 2013). Our results do not resolve this question, but we add to the picture that the network mechanism distributes firing patterns differentially according to cell type.

Conclusions

We conclude that the anatomical identity of the neuron is a strong determinant of the firing pattern. Analysis of burstiness, theta cycle skipping, and phase precession jointly suggest similarities between layer 3 cells and layer 2 stellate cells on one hand and layer 2 pyramidal cells and parasubicular cells on the other hand.

EXPERIMENTAL PROCEDURES

All experimental procedures were performed according to the German guidelines on animal welfare under the supervision of local ethics committees.

Juxtacellular Recordings and Immunohistochemistry

In this paper, we analyzed a dataset of juxtacellular recordings from the superficial medial entorhinal cortex and the parasubiculum that we have published previously (Ray et al., 2014; Tang et al., 2014a, 2015, 2016). Detailed descriptions of recording procedures (Pinault, 1996; Lee et al., 2006; Herfst et al., 2012; Tang et al., 2014b), quality control (Joshua et al., 2007), tissue preparation, immunohistochemistry, and image acquisition (Naumann et al., 2016; Ray and Brecht, 2016), can be found in these papers and in the Supplemental Experimental Procedures.

Classification of Non-identified Layer 2 Neurons

In addition to labeled cells, we included a number of unlabeled, regularly spiking cells from MEC L2 in our analysis. These cells were assigned as either putatively calbindin-positive (pCb+) pyramidal cells or putatively calbindin-negative (pCb−) stellate cells based on their theta strength and preferred theta phase angle using the classification approach of Tang et al. (2014a); i.e., based on the theta strength and preferred theta phase angle of spiking activity. As in Tang et al. (2014a), we used a 0.1 guard zone and found that the cells were well separated with no cells in the guard zone (Figure S1). In the manuscript, we refer to the pooled groups of identified and putative calbindin-positive pyramidal cells simply as "MEC L2 pyramids" and identified putative calbindin-negative stellate cells as "MEC L2 stellates." When we show example cells of the four cell types (Figures 1A and 1B and 6A–6C), we show only identified Cb+/− cells. In Figures S3 and S5, we show analysis of a dataset where we only included identified cells.

Analysis of Burstiness

To determine whether a neuron was discharging in a bursty pattern, we analyzed the ISI histogram using a similar approach as Latuske et al. (2015). ISIs below 60 ms were binned in 2-ms bins and normalized to area = 1 to generate a probability distribution (Figure 2A). A principle component analysis (PCA) was done on a matrix of the ISI probability distribution of all neurons ("pca" in MATLAB, MathWorks). For plotting, the density of cells in this space was estimated with a 2D Gaussian kernel density estimator ("kde2d"; Botev et al., 2010). The neurons were assigned to two clusters using a *k*-means clustering algorithm on the first three principal components ("kmeans"; MATLAB; Figure 2C, top). To assess the separation quality of the two clusters, we calculated the projection of the neurons onto Fisher's linear discriminant (the burstiness, using "LDA" from Scikit-Learn in Python) and found that the two clusters (non-bursty and bursty) were well separated with little overlap (Figure 2C, top). To check whether the distribution of burstiness was bimodal, thus reflecting two distinct classes of ISI histograms, we fitted probability density functions for Gaussian mixture models with between one and three underlying Gaussians and compared the models using the Akaike information criterion (Akaike 1974; AIC from "gmdistribution.fit" in MATLAB). A bimodal distribution best explained the data ($AIC_{unimodal}$ = 622.7, $AIC_{bimodal}$ = 609.6, $AIC_{trimodal}$ = 614.7). Based on the mean and variance of the two Gaussian distributions underlying the observed distribution of burstiness (Figure 2C, bottom, dashed red lines), we estimated that excluding cells where $-0.4 <$ burstiness < 1.5 would yield >95% correct labeling of non-bursty and bursty neurons in the non-bursty and bursty categories and used this as a guard zone (Latuske et al., 2015).

Analysis of Spike Shape

During recording, the juxtacellular traces were digitized at 20 kHz. To analyze the spike shapes, we first zero-phased high pass-filtered the raw signal at 100 Hz with a finite impulse response filter of order 2^8 ("fir1" in MATLAB). The spike times were detected by thresholding the filtered signal and saving each threshold crossing ± 2.5 ms. Spike sorting based on the first principal components was performed on these 5-ms snippets to remove any threshold crossings because of artifacts in the signal (Tang et al., 2014a). To align the spike shapes optimally after spike sorting, the 5-ms snippets were oversampled at five times their original sampling rate using a spline interpolation ("interp1" in MATLAB) and were then aligned to the peak sample. To ensure that we were only analyzing shapes free of distortions because of drift of the pipette and that the spikes were well above the noise floor, we only analyzed spikes for which the spike amplitude was in the top 60^{th}-90^{th} percentile and where the *Z* score of the spike amplitude was >17. The noise floor was defined as the mean of the first and last 0.5 ms of each 5-ms spike snippet. We also removed any spikes where there was another spike in the preceding 100 ms. In the four cell groups, there were only a few cells where the spikes did not have sufficient quality to analyze the spike shape, and we could analyze 19/22 parasubicular cells, 24/31 MEC L2 pyramidal cells, 58/68 MEC L2 stellate cells, and 27/32 MEC L3 cells. We calculated the mean spike shape of every cell and determined the spike features from these traces. For plotting the comparison between cells and for illustrating the differences in peak-to-trough time (Figures 4A and 4B), we normalized the spike shape by subtracting the noise floor, dividing the mean spike by the peak-to-trough height, and setting the peak height to 1.

Analysis of Theta Rhythmicity and Theta Cycle Skipping

To determine whether a neuron was rhythmic and theta cycle-skipping, we used an MLE of a parametric model of the ISI histogram ("mle_rhythmicity"; Climer et al., 2015). For every cell, we fitted three models to the ISI distribution: a flat model with no rhythmic components, a rhythmic, non-skipping model with a rhythmic modulation of the ISI histogram, and a rhythmic, cycle-skipping

model with a rhythmic modulation of the ISI histogram and a second parameter introducing theta cycle skipping (i.e., a higher amplitude of every other peak in the ISI histogram). When fitting the models, we searched for a rhythmic component with a theta frequency between 5 and 13 Hz and for cycle skippings >0.01. The three fitted models were compared using the appropriate χ^2 statistic (calculated from the maximum log likelihood of the models) to generate two p values: $p_{rhythmic}$ (comparing the flat and the rhythmic, non-skipping models) and $p_{skipping}$ (comparing the rhythmic, non-skipping and the rhythmic, cycle-skipping models). The cells were classified using a two-level classification (Figure 5B). First we determined whether a cell was rhythmic ($p_{rhythmic} < 0.05$) or non-rhythmic ($p_{rhythmic} > 0.05$). Then we classified the rhythmic cells as either rhythmic, cycle-skipping ($p_{skipping} < 0.05$) or rhythmic, non-skipping ($p_{skipping} > 0.05$).

To statistically assess whether theta cycle skipping cells were rarer among rhythmic cells in the generally non-rhythmic cell types (MEC L2 stellates and MEC L3 neurons) than in the generally rhythmic cell types (parasubicular neurons and MEC L2 pyramids), we fitted a mixed-effects logistic regression. We constructed a vector, isGenRhytm (which takes the value 1 for parasubicular neurons and MEC L2 pyramids and the value 0 for MEC L2 stellates and MEC L3 neurons). We also constructed a vector type that simply dummy-coded the four neuron types from 1, 2, 3, and 4. We dummy-coded when the neuron was theta cycle-skipping in the vector isSkipping. We then modeled the probability of being rhythmic as a function of being generally rhythmic while controlling for the different number of cells in the four categories of neurons: "isSkipping~isGenRhytm + (1|type)" using "fitglme" in MATLAB (Aarts et al., 2014).

In addition to the MLE approach, we also calculated the theta strength and preferred theta phase of every cell. The local field potential was bandpass-filtered in the theta range (4–12 Hz), and a Hilbert transform was used to determine the instantaneous phase of the theta wave for every spike. The theta locking strength and the preferred phase angle were calculated as the modulus and argument of the Rayleigh average vector of the theta phase at all spike times.

Statistical Modeling

Statistical modeling (generalized linear models) was done in MATLAB using the "glmefit" function. We modeled burstiness as a function of theta strength as a normally distributed variable (Figures S3A–S3C). We modeled the peak-to-trough time as a gamma-distributed variable with a reciprocal link function in MATLAB because it can only assume positive values (Figures S4A–S4C). To compare models, we either calculated and compared the AIC (Akaike, 1974) or, in the case of nested models, calculated the p value from likelihood ratio tests. In the manuscript, we describe all statistical models using standard Wilkinson notation (Wilkinson and Rogers, 1973).

Analysis of Phase Precession

To identify coherent periods of elevated firing ("single runs"), we follow a previously applied strategy based on the temporal structure of the recorded spike trains (Reifenstein et al., 2016). Briefly, we convolved the spike train with a Gaussian kernel to estimate the instantaneous firing rate. We then used a firing rate threshold to locate periods of elevated firing (Figure 6A, top). For each of the single runs, the times and theta phases of all spikes were used to assess phase precession. We quantified phase precession by calculating the slope, phase range, and circular-linear correlation coefficient of the circular-linear regression line (Figure 6A, bottom; Kempter et al., 2012; Reifenstein et al., 2012, 2014, 2016).

SUPPLEMENTAL INFORMATION

Supplemental Information includes Supplemental Experimental Procedures and five figures and can be found with this article online at http://dx.doi.org/10.1016/j.celrep.2016.06.057.

AUTHOR CONTRIBUTIONS

C.L.E. analyzed burstiness, spike shape, theta rhythmicity, and cycle skipping. E.T.R. analyzed phase precession. Q.T. and A.B. provided access to juxtacellular data and assisted with data analysis. S.R. performed immunohistochemistry and microscopy. S.S., R.K., and M.B. provided expertise and feedback on the analysis and supervised the project. C.L.E. conceived the study and wrote the first version of the manuscript. All authors provided feedback and contributed to writing the manuscript.

ACKNOWLEDGMENTS

This work was supported by the Humboldt Universität zu Berlin, BCCN Berlin (German Federal Ministry of Education and Research BMBF, Förderkennzeichen 01GQ1001A, 01GQ0901, 01GQ1403, and 01GQ0972), NeuroCure, the Neuro-Behavior ERC grant, and the Gottfried Wilhelm Leibniz Prize of the DFG. We thank Andreea Neukirchner, Juliane Steger, and Undine Schneeweiß for technical assistance.

Received: March 30, 2016
Revised: May 4, 2016
Accepted: June 12, 2016
Published: July 14, 2016

REFERENCES

Aarts, E., Verhage, M., Veenvliet, J.V., Dolan, C.V., and van der Sluis, S. (2014). A solution to dependency: using multilevel analysis to accommodate nested data. Nat. Neurosci. *17*, 491–496.

Akaike, H. (1974). A new look at the statistical model identification. IEEE Trans. Automat. Contr. *19*, 716–723.

Alessi, C., Raspanti, A., and Magistretti, J. (2016). Two Distinct Types of Depolarizing Afterpotentials are Differentially Expressed in Stellate and Pyramidal-like Neurons of Entorhinal-Cortex Layer II. Hippocampus.

Alonso, A., and Klink, R. (1993). Differential electroresponsiveness of stellate and pyramidal-like cells of medial entorhinal cortex layer II. J. Neurophysiol. *70*, 128–143.

Boccara, C.N., Sargolini, F., Thoresen, V.H., Solstad, T., Witter, M.P., Moser, E.I., and Moser, M.B. (2010). Grid cells in pre- and parasubiculum. Nat. Neurosci. *13*, 987–994.

Botev, Z.I., Grotowaki, J.F., and Kroese, D.P. (2010). Kernel density estimation via diffusion. Ann. Stat. *38*, 2916–2957.

Brandon, M.P., Bogaard, A.R., Schultheiss, N.W., and Hasselmo, M.E. (2013). Segregation of cortical head direction cell assemblies on alternating θ cycles. Nat Neurosci. *16*, 739–748.

Brecht, M., Ray, S., Burgalossi, A., Tang, Q., Schmidt, H., and Naumann, R. (2013). An isomorphic mapping hypothesis of the grid representation. Philos. Trans. R. Soc. Lond. B Biol. Sci. *369*, 20120521.

Burgalossi, A., Herfst, L., von Heimendahl, M., Förste, H., Haskic, K., Schmidt, M., and Brecht, M. (2011). Microcircuits of functionally identified neurons in the rat medial entorhinal cortex. Neuron *70*, 773–786.

Burgess, N. (2014). The 2014 Nobel Prize in Physiology or Medicine: a spatial model for cognitive neuroscience. Neuron *84*, 1120–1125.

Climer, J.R., DiTullio, R., Newman, E.L., Hasselmo, M.E., and Eden, U.T. (2015). Examination of rhythmicity of extracellularly recorded neurons in the entorhinal cortex. Hippocampus *25*, 460–473.

Csicsvari, J., Hirase, H., Czurkó, A., Mamiya, A., and Buzsáki, G. (1999). Oscillatory coupling of hippocampal pyramidal cells and interneurons in the behaving Rat. J. Neurosci. *19*, 274–287.

Domnisoru, C., Kinkhabwala, A.A., and Tank, D.W. (2013). Membrane potential dynamics of grid cells. Nature *495*, 199–204.

Fuchs, E.C., Neitz, A., Pinna, R., Melzer, S., Caputi, A., and Monyer, H. (2016). Local and Distant Input Controlling Excitation in Layer II of the Medial Entorhinal Cortex. Neuron *89*, 194–208.

Giocomo, L.M., Moser, M.-B., and Moser, E.I. (2011). Computational models of grid cells. Neuron *71*, 589–603.

Glasgow, S.D., and Chapman, C.A. (2008). Conductances mediating intrinsic theta-frequency membrane potential oscillations in layer II parasubicular neurons. J. Neurophysiol. *100*, 2746–2756.

Gold, C., Girardin, C.C., Martin, K.A., and Koch, C. (2009). High-amplitude positive spikes recorded extracellularly in cat visual cortex. J. Neurophysiol. *102*, 3340–3351.

Hafting, T., Fyhn, M., Molden, S., Moser, M.B., and Moser, E.I. (2005). Microstructure of a spatial map in the entorhinal cortex. Nature *436*, 801–806.

Hafting, T., Fyhn, M., Bonnevie, T., Moser, M.B., and Moser, E.I. (2008). Hippocampus-independent phase precession in entorhinal grid cells. Nature *453*, 1248–1252.

Herfst, L., Burgalossi, A., Haskic, K., Tukker, J.J., Schmidt, M., and Brecht, M. (2012). Friction-based stabilization of juxtacellular recordings in freely moving rats. J. Neurophysiol. *108*, 697–707.

Jaramillo, J., Schmidt, R., and Kempter, R. (2014). Modeling inheritance of phase precession in the hippocampal formation. J. Neurosci. *34*, 7715–7731.

Jeewajee, A., Barry, C., Douchamps, V., Manson, D., Lever, C., and Burgess, N. (2013). Theta phase precession of grid and place cell firing in open environments. Philos. Trans. R Soc. Lond. B Biol. Sci. *369*, 20120532.

Joshua, M., Elias, S., Levine, O., and Bergman, H. (2007). Quantifying the isolation quality of extracellularly recorded action potentials. J. Neurosci. Methods *163*, 267–282.

Kempter, R., Leibold, C., Buzsáki, G., Diba, K., and Schmidt, R. (2012). Quantifying circular-linear associations: hippocampal phase precession. J. Neurosci. Methods *207*, 113–124.

Kinkhabwala AA, Aronov D, Tank DW (2015) Visual cue-related activity of MEC cells during navigation in virtual reality. Program No. 632.21/CC2. 2015 Neuroscience Meeting Planner. Washington, DC: Society for Neuroscience, 2015. Online.

Kitamura, T., Pignatelli, M., Suh, J., Kohara, K., Yoshiki, A., Abe, K., and Tonegawa, S. (2014). Island cells control temporal association memory. Science *343*, 896–901.

Koenig, J., Linder, A.N., Leutgeb, J.K., and Leutgeb, S. (2011). The spatial periodicity of grid cells is not sustained during reduced theta oscillations. Science *332*, 592–595.

Kropff, E., Carmichael, J.E., Moser, M.B., and Moser, E.I. (2015). Speed cells in the medial entorhinal cortex. Nature *523*, 419–424.

Latuske, P., Toader, O., and Allen, K. (2015). Interspike Intervals Reveal Functionally Distinct Cell Populations in the Medial Entorhinal Cortex. J. Neurosci. *35*, 10963–10976.

Lee, A.K., Manns, I.D., Sakmann, B., and Brecht, M. (2006). Whole-cell recordings in freely moving rats. Neuron *51*, 399–407.

Lever, C., Burton, S., Jeewajee, A., O'Keefe, J., and Burgess, N. (2009). Boundary vector cells in the subiculum of the hippocampal formation. J. Neurosci. *29*, 9771–9777.

Mizuseki, K., Sirota, A., Pastalkova, E., and Buzsáki, G. (2009). Theta oscillations provide temporal windows for local circuit computation in the entorhinal-hippocampal loop. Neuron *64*, 267–280.

Mountcastle, V.B., Talbot, W.H., Sakata, H., and Hyvärinen, J. (1969). Cortical neuronal mechanisms in flutter-vibration studied in unanesthetized monkeys. Neuronal periodicity and frequency discrimination. J. Neurophysiol. *32*, 452–484.

Naumann, R.K., Ray, S., Prokop, S., Las, L., Heppner, F.L., and Brecht, M. (2016). Conserved size and periodicity of pyramidal patches in layer 2 of medial/caudal entorhinal cortex. J. Comp. Neurol. *524*, 783–806.

Newman, E.L., and Hasselmo, M.E. (2014). Grid cell firing properties vary as a function of theta phase locking preferences in the rat medial entorhinal cortex. Front. Syst. Neurosci. *8*, 193.

Pastoll, H., Ramsden, H.L., and Nolan, M.F. (2012). Intrinsic electrophysiological properties of entorhinal cortex stellate cells and their contribution to grid cell firing fields. Front. Neural Circuits *6*, 17.

Pinault, D. (1996). A novel single-cell staining procedure performed in vivo under electrophysiological control: morpho-functional features of juxtacellularly labeled thalamic cells and other central neurons with biocytin or Neurobiotin. J. Neurosci. Methods *65*, 113–136.

Ray, S., and Brecht, M. (2016). Structural development and dorsoventral maturation of the medial entorhinal cortex. eLife *5*, 13343.

Ray, S., Naumann, R., Burgalossi, A., Tang, Q., Schmidt, H., and Brecht, M. (2014). Grid-layout and theta-modulation of layer 2 pyramidal neurons in medial entorhinal cortex. Science *343*, 891–896.

Reifenstein, E.T., Kempter, R., Schreiber, S., Stemmler, M.B., and Herz, A.V. (2012). Grid cells in rat entorhinal cortex encode physical space with independent firing fields and phase precession at the single-trial level. Proc. Natl. Acad. Sci. USA *109*, 6301–6306.

Reifenstein, E., Stemmler, M., Herz, A.V.M., Kempter, R., and Schreiber, S. (2014). Movement dependence and layer specificity of entorhinal phase precession in two-dimensional environments. PLoS ONE *9*, e100638.

Reifenstein, E.T., Ebbesen, C.L., Tang, Q., Brecht, M., Schreiber, S., and Kempter, R. (2016). Cell-Type Specific Phase Precession in Layer II of the Medial Entorhinal Cortex. J. Neurosci. *36*, 2283–2288.

Sargolini, F., Fyhn, M., Hafting, T., McNaughton, B.L., Witter, M.P., Moser, M.B., and Moser, E.I. (2006). Conjunctive representation of position, direction, and velocity in entorhinal cortex. Science *312*, 758–762.

Schmidt, R., Diba, K., Leibold, C., Schmitz, D., Buzsáki, G., and Kempter, R. (2009). Single-trial phase precession in the hippocampus. J. Neurosci. *29*, 13232–13241.

Sheffield, M.E.J., and Dombeck, D.A. (2015). The binding solution? Nat. Neurosci. *18*, 1060–1062.

Solstad, T., Boccara, C.N., Kropff, E., Moser, M.B., and Moser, E.I. (2008). Representation of geometric borders in the entorhinal cortex. Science *322*, 1865–1868.

Sun, C., Kitamura, T., Yamamoto, J., Martin, J., Pignatelli, M., Kitch, L.J., Schnitzer, M.J., and Tonegawa, S. (2015). Distinct speed dependence of entorhinal island and ocean cells, including respective grid cells. Proc. Natl. Acad. Sci. USA *112*, 9466–9471.

Tang, Q., Burgalossi, A., Ebbesen, C.L., Ray, S., Naumann, R., Schmidt, H., Spicher, D., and Brecht, M. (2014a). Pyramidal and stellate cell specificity of grid and border representations in layer 2 of medial entorhinal cortex. Neuron *84*, 1191–1197.

Tang, Q., Brecht, M., and Burgalossi, A. (2014b). Juxtacellular recording and morphological identification of single neurons in freely moving rats. Nat. Protoc. *9*, 2369–2381.

Tang, Q., Ebbesen, C.L., Sanguinetti-Scheck, J.I., Preston-Ferrer, P., Gundlfinger, A., Winterer, J., Beed, P., Ray, S., Naumann, R., Schmitz, D., et al. (2015). Anatomical Organization and Spatiotemporal Firing Patterns of Layer 3 Neurons in the Rat Medial Entorhinal Cortex. J. Neurosci. *35*, 12346–12354.

Tang, Q., Burgalossi, A., Ebbesen, C.L., Sanguinetti-Scheck, J.I., Schmidt, H., Tukker, J.J., Naumann, R., Ray, S., Preston-Ferrer, P., Schmitz, D., and Brecht, M. (2016). Functional Architecture of the Rat Parasubiculum. J. Neurosci. *36*, 2289–2301.

Unal, G., Joshi, A., Viney, T.J., Kis, V., and Somogyi, P. (2015). Synaptic Targets of Medial Septal Projections in the Hippocampus and Extrahippocampal Cortices of the Mouse. J. Neurosci. *35*, 15812–15826.

Varga, C., Lee, S.Y., and Soltesz, I. (2010). Target-selective GABAergic control of entorhinal cortex output. Nat. Neurosci. *13*, 822–824.

Welday, A.C., Shlifer, I.G., Bloom, M.L., Zhang, K., and Blair, H.T. (2011). Cosine directional tuning of theta cell burst frequencies: evidence for spatial coding by oscillatory interference. J. Neurosci. *31*, 16157–16176.

Wilkinson, G.N., and Rogers, C.E. (1973). Symbolic Description of Factorial Models for Analysis of Variance. J. R. Stat. Soc. Ser. C Appl. Stat. *22*, 392–399.

Winter, S.S., Clark, B.J., and Taube, J.S. (2015). Spatial navigation. Disruption of the head direction cell network impairs the parahippocampal grid cell signal. Science *347*, 870–874.

Zilli, E.A. (2012). Models of grid cell spatial firing published 2005-2011. Front. Neural Circuits *6*, 16.